Physics in Medicine & Biology

PAPER

Recovery of inter-detector and inter-crystal scattering in brain PET based on LSO and GAGG crystals

To cite this article: Seungeun Lee *et al* 2020 *Phys. Med. Biol.* **65** 195005

IOP Publishing Phys. Med. Biol. 65 (2020) 195005 https://doi.org/10.1088/1361-6560/ab9f5c

Physics in Medicine & Biology

IPEM Institute of Physics and Engineering in Medicine

CrossMark

RECEIVED
5 March 2020

REVISED
7 June 2020

ACCEPTED FOR PUBLICATION
23 June 2020

PUBLISHED
23 September 2020

PAPER

Recovery of inter-detector and inter-crystal scattering in brain PET based on LSO and GAGG crystals

Seungeun Lee[1,2], **Kyeong Yun Kim**[1,2,3], **Min Sun Lee**[2] **and Jae Sung Lee**[1,2,3]

[1] Department of Biomedical Sciences, Seoul National University, Seoul 03080, Republic of Korea
[2] Department of Nuclear Medicine, Seoul National University, Seoul 03080, Republic of Korea
[3] Brightonix Imaging Inc., Seoul 04782, Republic of Korea

E-mail: jaes@snu.ac.kr

Keywords: inter-detector scattering, inter-crystal scattering, Monte Carlo simulation, image quality, PET

Abstract

Gadolinium aluminum gallium garnet (GAGG) is a promising scintillator crystal for positron emission tomography (PET) detectors owing to its advantages of energy resolution, light yield, and absence of intrinsic radiation. However, a large portion of the incident photons undergoes Compton scattering within GAGG crystal because of its low stopping power compared to that of lutetium-based crystals such as Lu_2SiO_5 (LSO). Inter-detector scattering (IDS) and inter-crystal scattering (ICS) result in loss of sensitivity and image quality of PET, respectively. We performed a Monte Carlo simulation study to evaluate IDS recovery in our currently developing brain-dedicated PET, and extended the idea to ICS recovery. We also compared the impact of the recoveries on LSO- and GAGG-based PET scanners. We measured the sensitivity and spatial resolution of the brain PET, and analyzed the image quality using a lesion phantom, a hot-rod phantom, and a 2D Hoffman phantom with applying IDS or ICS recovery. IDS recovery increased the PET sensitivity and improved the noise level of the reconstructed images. ICS recovery enhanced the spatial resolution and the contrast of the images was improved. As the occurrence rates of IDS and ICS were higher in GAGG than in LSO, the overall impact of IDS or ICS recovery was significant in GAGG. In conclusion, we showed that the proportional method would be suitable for IDS and ICS recoveries of PET, and emphasized the importance of ICS and IDS recoveries for PET using crystals with low stopping power.

1. Introduction

Gadolinium aluminum gallium garnet (GAGG; $Gd_3Al_2Ga_3O_{12}$) is one of the most promising candidates of crystal materials for positron emission tomography (PET) detectors owing to its several advantages compared to lutetium-based crystals which are the most widely used (table 1). GAGG with 1% cerium-doping has a 40% higher light yield than Lu_2SiO_5 (LSO) and better intrinsic energy resolution (Kamada *et al* 2012, Yeom *et al* 2013, Lee *et al* 2016, Stewart *et al* 2016, Kobayashi *et al* 2017). As GAGG does not have intrinsic radiation, a wide range of photon energy spectra is reliably measurable. Photosensors with quantum efficiency matched to the peak wavelength of GAGG, approximately 530 nm, are available in the market (Frach *et al* 2009, Ferri *et al* 2014).

However, the main limit of GAGG is its low stopping power. Both the density and effective atomic number of GAGG are lower than those of LSO. The cross section of the 511 keV photon interaction is a function of the density and effective atomic number of the material. Compared to LSO, the cross section of photoelectric absorption is low while that of Compton scattering is high in GAGG (Berger *et al* 2010). Therefore, the proportion of Compton scattering among the photon interaction types is expected to be large if we use GAGG crystals for PET detectors.

Compton scattering within the PET detector elements is an unfavorable type of photon interaction. Inter-detector scattering (IDS) is a type of triple coincidence with photon Compton scatters from a detector block to an adjacent block (figure 1(a)). IDS results in loss of sensitivity because multiple coincidences are

Table 1. Physical properties of LSO and GAGG.

	LSO	GAGG
Light yield (photons MeV^{-1})[a]	32 000	46 000
Intrinsic energy resolution at 662 keV (%)[a]	7.9	5.2
Intrinsic radiation	Yes	No
Density (g cm^{-3})[a]	7.40	6.63
Effective atomic number (Z_{eff})[a]	64	54
Cross section of photoelectric absorption of 511 keV photon (10^{-2} cm^2 g^{-1})[b]	3.84	1.88
Cross section of Compton scattering of 511 keV photon (10^{-2} cm^2 g^{-1})[b]	7.29	7.51
Decay time (ns)[a]	41	90

[a] Stewart *et al* 2016, Kamada *et al* 2012 (C&A corporation, Japan)

[b] Berger *et al* 2010, no doping was considered.

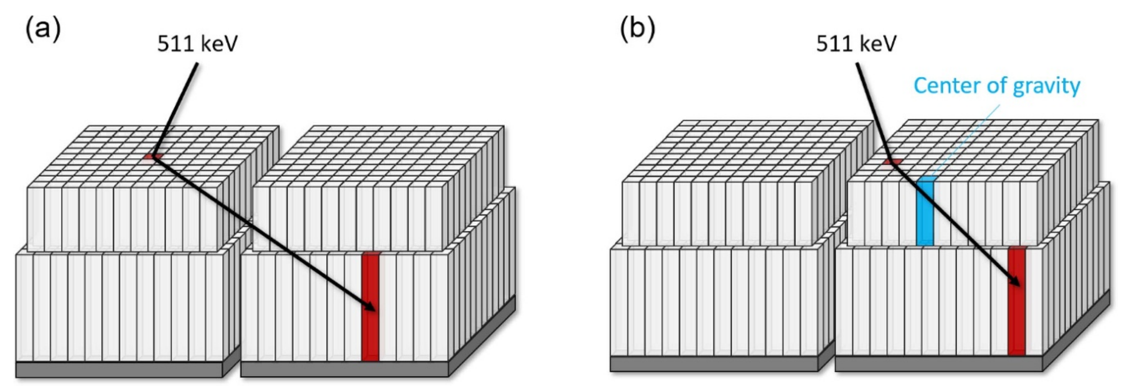

Figure 1. Schematic of Compton scattering within PET detectors. (a) IDS, (b) ICS.

practically rejected during PET data acquisition. Inter-crystal scattering (ICS) is a Compton scattering of a photon from a crystal to another crystal within a single block (figure 1(b)). In practical PET systems that use charge sharing for crystal readout such as charge division circuits, the crystal is positioned based on the center of gravity (COG) of the deposited energies within a block (Siegel *et al* 1996, Kwon *et al* 2011). However, for ICS events, the crystal positioned by COG is likely to be different from the actual earliest-interacted crystal. The LORs are incorrectly drawn by crystal mispositioning eventually degrading PET image quality.

Several groups have studied the effect of IDS and ICS on PET performance (e.g. Teimoorisichani and Goertzen 2019, Zhang *et al* 2019). Great efforts have been made to develop algorithms that recover IDS or ICS events rejected or ignored in conventional approaches. Studies related to IDS recovery usually focus on sensitivity increase by adding the recovered IDS events to the practical double coincidences (Wagadarikar *et al* 2012, Yoshida *et al* 2014, Lage *et al* 2015, Michaud *et al* 2015). ICS recovery studies prove the enhancement of resolution (Comanor *et al* 1996, Shao *et al* 1996, Rafecas *et al* 2003, Pratx and Levin 2009, Gillam *et al* 2014, Abbaszadeh *et al* 2018, Surti and Karp 2018, Lee *et al* 2018a, Hsu *et al* 2019). However, optimization of the recovery algorithm is still under investigation because the occurrences of IDS and ICS depend on PET geometry, and the impact of the recoveries on image quality is not fully understood. In addition, as both IDS and ICS are driven by Compton scattering, recoveries of IDS and ICS are potentially likely to be integrated.

The three main goals of this study were (1) to apply IDS recovery to brain PET, (2) to extend the IDS recovery method to ICS recovery, and (3) to compare the impact of IDS and ICS recoveries on the image quality of PET systems made of different crystal materials.

In our previous work, we evaluated several IDS recovery methods in a small-animal PET (Lee *et al* 2018b). The proportional method (Lage *et al* 2015), which is explained in section 2.2.1, yielded a good signal-to-noise ratio and contrast of the reconstructed images compared to those of other methods. In addition, the proportional method has some advantages. For example, it does not require energy information for the recovery, and it is independent of the depth-of-interaction (DOI) measurement capability or energy resolution of the PET system. As the occurrence of IDS is highly dependent on PET geometry, the impact of IDS recovery on a brain-sized PET was investigated.

We applied the same IDS recovery method to ICS of the double coincidences by considering each crystal as a detector block of IDS events. The system was assumed to be capable of reading out the individual interacted crystals of the ICS events within single blocks. The feasibility of the proportional method for ICS recovery was evaluated by comparing it with the performance using COG.

To investigate the dependence of the performance impact of IDS or ICS recovery on the crystal stopping power, we applied IDS and ICS recoveries to PET scanners made of LSO and GAGG crystals. Different crystal materials would result in different distributions of the photoelectric absorption and Compton scattering of the photons. We quantitatively assessed the impact of the recoveries on image quality and compared their degree of impact on LSO and GAGG PET.

2. Materials and methods

2.1. Simulation

We conducted a GATE v7.0 Monte Carlo simulation (Jan *et al* 2004) to build up the PET scanner and acquire the phantom data.

2.1.1. PET system setup

The simulated scanner for brain imaging had axial field-of-view and inner diameter of the scanner of 10 and 33 cm, respectively. The scanner was composed of 18 sectors in a cylindrical arrangement, and each sector consisted of 2 (transaxial) $\times$ 4 (axial) crystal blocks. A crystal block consisted of 11 $\times$ 11 crystals in the upper layer and 12 $\times$ 12 crystals in the lower layer, which were in a dual-layered offset arrangement for DOI measurement. The sizes of the crystals were 2.09 $\times$ 2.09 $\times$ 8 mm^3 and 2.09 $\times$ 2.09 $\times$ 12 mm^3 in the upper and lower layers, respectively, while the crystal pitch was 2.17 mm. The size of the gap between the blocks in a sector was identical to that of one crystal pitch. Under the same geometrical conditions, we tested LSO (Lu_2SiO_5, density = 7.4 g cm^{-3}) and GAGG ($Gd_3Al_2Ga_3O_{12}$, density = 6.63 g cm^{-3}) as crystal materials. As optical simulation was not conducted in this study, crystal doping was not considered.

For the system readout setup, the energy resolutions of LSO and GAGG PET at 511 keV were set to 10% and 6% in full width half maximum (FWHM), respectively. The energy resolution for each energy was inversely proportional to square root of deposited energy. From the *Singles* output files of GATE, we sorted the single events and applied a coincidence time window of 4 ns. The double and triple coincidences were recorded separately, counting the interacted crystal blocks for each event. An energy window of [350, 650] keV was applied to the double coincidences. The interacted crystals were read out individually. COG positioning was performed by weighting the deposited energies to the x–y coordinates of the centers of the involved crystals on the flood map. Then, the crystal which was the nearest to the energy-weighted position was assigned as the interacted crystal.

2.1.2. Simulation setup for performance measurement

2.1.2.1. IDS and ICS occurrence rates

A 511 keV back-to-back rod source was placed along the axial center of the scanner to measure the occurrence rates of IDS and ICS according to NEMA NU2-2007 (National Electrical Manufacturers Association 2007). The activity was 0.1 MBq, and the diameter and length of the source were 1 mm and 70 cm, respectively. The acquisition time was 50 min.

We measured the IDS occurrence rate by dividing the number of recovered IDS by the number of double coincidences. The ICS occurrence rate was calculated by dividing the number of ICS events by the total number of single events over the entire block. The crystal mispositioning rate was calculated as the proportion of single events positioned by COG to different crystals from the first interacted crystal owing to ICS among the total number of single events. The ICS occurrence rate and the crystal mispositioning rate were measured for both 511 keV (i.e. non-IDS) and IDS photons.

2.1.2.2. Spatial resolution

To measure the spatial resolution, we used a 100 MBq ^{18}F point source within a plastic cylinder with a diameter and length of 6 mm to cover the maximum positron range of ^{18}F. The source was placed at the radial offsets of 1–13 cm with a step size of 3 cm in the axial center of the scanner. A cylindrical warm uniform background, consisted of 511 keV back-to-back source with an activity concentration contrast of 0.1 and a geometry identical to the plastic cylinder, was added around the point source for reliability. For each reconstructed point source image, we measured the radial, tangential, and axial resolutions in FWHM.

2.1.2.3. Image quality

We designed a brain-sized phantom based on the NEMA IEC body phantom for quantitative evaluation of the image quality, as shown in figure 2(a) (National Electrical Manufacturers Association 2007). Inside a cylindrical background region with an activity concentration of 5.3 kBq cc^{-1} of 511 keV back-to-back

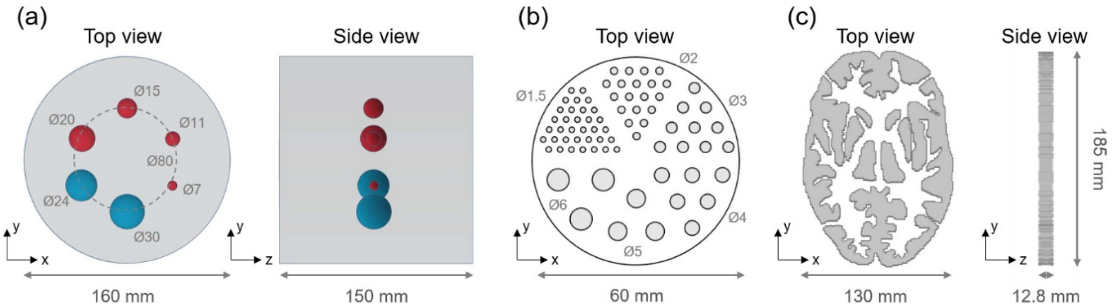

Figure 2. Simulated phantoms for image quality evaluation. (a) Lesion phantom. The red, blue, gray regions correspond to hot lesions, cold lesions, and background, respectively. (b) Hot-rod phantom. (c) 2D Hoffman brain phantom. The source was uniformly distributed over the gray-colored regions in (b) and (c).

source, hot and cold spherical lesions with different diameters were arranged in a circle at the axial center. The activity concentration of the hot lesions was three times higher than that of the background region. The phantom was filled with water.

We also imaged a Derenzo-like hot-rod phantom (figure 2(b)) and 2D Hoffman voxelized phantom (figure 2(c)) to investigate the visibility of the fine structure. The hot-rod phantom contained ^{18}F rods which had diameters from 1.5 mm to 6 mm and a length of 6 mm in common inside a water cylinder. The thickness of the Hoffman phantom was 12.8 mm, and the 511 keV back-to-back source was distributed in the shape of the brain filled with acryl.

2.2. IDS and ICS recovery

Four different recovery types were compared throughout the study: non-recovered, IDS-recovered, ICS-recovered, and ICS/IDS-recovered. When the IDS recovery was not applied, only double coincidences were used. When the ICS recovery was not applied, a COG crystal readout was used for each block.

To simplify, multiple coincidences with more than three detector blocks were rejected in IDS recovery. In the case of ICS, only the first two interacted crystals were considered, and the energy depositions after the first crystal were assumed to be deposited in the second crystal. This simplification is reasonable because proportion of ICS involving two crystals (i.e. 1 scattering) are dominant among total ICS (i.e. ⩾1 scattering) of 511 keV photons (80% in LSO, 72% in GAGG).

2.2.1. IDS recovery

Certain criteria were applied to the triple coincidences to determine whether they were IDS events or not (figure 3). For three blocks where the photon interactions occurred in a triple coincidence, the transaxial block number differences between the block pairs were measured. If the minimum block difference (BD_{min}) was smaller than a certain threshold (d), the corresponding block pair was considered as the block where the scattered photon was detected (S_1 and S_2), and the remaining interaction was considered as photoelectric absorption (P). If BD_{min} was larger than the threshold, the block with the largest energy deposited was considered as the photoelectric absorption block. The value d was optimized to maximize the accuracy of the discriminating P and S in our PET geometry by analyzing *Hits* output files from GATE. Energy window was then applied to validate that both energies of the photon pair are 511 keV.

The IDS recovery method we used in this study, the so-called 'proportional method,' distributed the IDS events with a weight proportional to the count of recorded non-IDS double coincidence of each LOR (Lage *et al* 2015). In the case shown in figure 4(a), the counts of the two LORs of PS_1 and PS_2 were calculated as follows:

$$LOR_{PS_k} = D_{PS_k} + \frac{D_{PS_k}}{D_{PS_1} + D_{PS_2}} IDS_{PS_1S_2} \text{ for } k \in \{1,\ 2\} \tag{1}$$

where *LOR*, *D*, and *IDS* denote number of LOR, non-IDS double coincidences, and IDS, respectively. The subscripts indicate the positions where each event is involved in. The numbered subscripts discriminate the interacted blocks with Compton scattering.

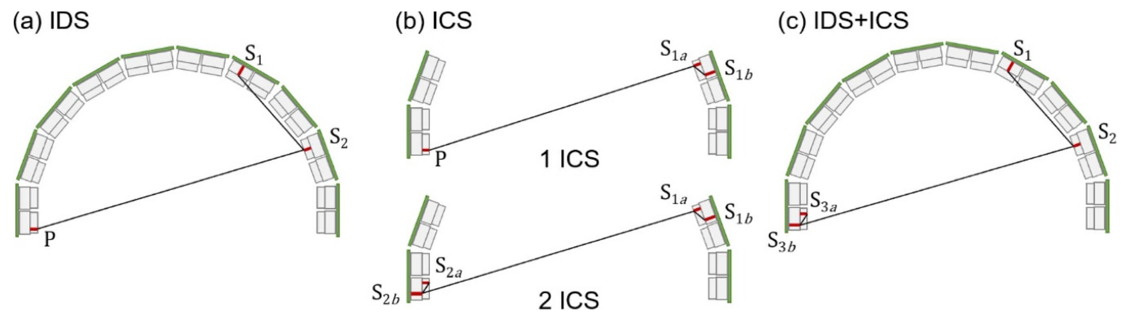

Figure 3. Types of recovered events. (a) Triple coincidences that were validated as IDS. (b) Double coincidences containing 1 or 2 ICS. (c) Triple coincidences where both IDS and ICS occurred. P and S denote the crystals interacted by photoelectric absorption and Compton scattering, respectively. The numbered subscripts discriminate the interacted blocks with Compton scattering, while the alphabetic subscripts denote the crystals where ICS was detected within a block.

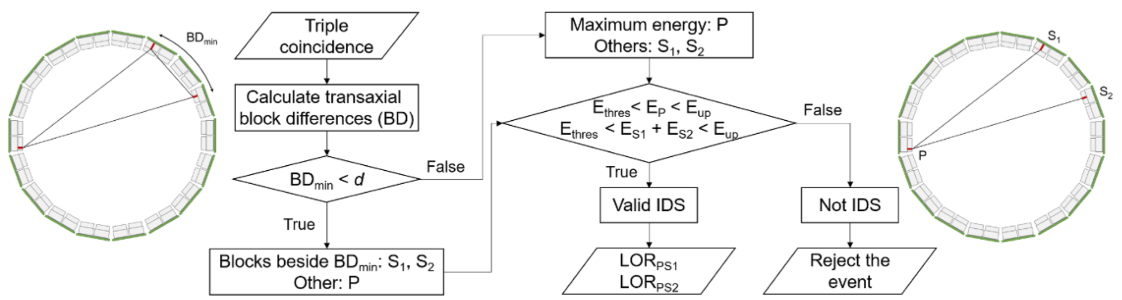

Figure 4. Algorithm to determine a triple coincidence as a valid IDS. Only valid IDS events were recovered and included for image reconstruction.

2.2.2. ICS recovery

We implemented the proportional method for ICS events by considering each crystal as a detector block of IDS events (figure 4(b)). Among the double coincidences, the number of ICS events (*ICS*) was proportionally distributed with the events in which both interactions were photoelectric absorption (*PE*).

Similar to equation (1), the counts of LORs in an event containing 1 ICS were calculated as follows:

$$LOR_{\mathrm{PS}_{1u}} = PE_{\mathrm{PS}_{1u}} + \frac{PE_{\mathrm{PS}_{1u}}}{PE_{\mathrm{PS}_{1a}} + PE_{\mathrm{PS}_{1b}}} ICS_{\mathrm{PS}_{1a}\mathrm{S}_{1b}} \text{ for } u \in \{a,\ b\}\,. \tag{2}$$

The counts of LORs in an event containing 2 ICS were calculated as follows:

$$\begin{gathered} LOR_{\mathrm{S}_{1u}\mathrm{S}_{2v}} = PE_{\mathrm{S}_{1u}\mathrm{S}_{2v}} + \frac{PE_{\mathrm{S}_{1u}\mathrm{S}_{2v}}}{PE_{\mathrm{S}_{1a}\mathrm{S}_{2a}} + PE_{\mathrm{S}_{1a}\mathrm{S}_{2a}} + PE_{\mathrm{S}_{1a}\mathrm{S}_{2a}} + PE_{\mathrm{S}_{1a}\mathrm{S}_{2a}}} ICS_{\mathrm{S}_{1a}\mathrm{S}_{1b}\mathrm{S}_{2a}\mathrm{S}_{2b}} \\ \text{for } (u,v) \in \{(a,a)\,,\,(a,b)\,,\,(b,a)\,,\,(b,b)\}\,. \end{gathered} \tag{3}$$

Please note that the alphabetic subscripts denote the crystals where ICS was detected within a block.

2.2.3. IDS/ICS recovery

We integrated the IDS and ICS recoveries to the triple coincidences that underwent both IDS and ICS and added to the ICS-recovered and IDS-recovered data (figure 4(c)). To simplify, only the IDS events that ICS occurred for non-IDS photons were recovered using an equation similar to (3):

$$\begin{gathered} LOR_{\mathrm{S}_{3u}\mathrm{S}_{k}} = PE_{\mathrm{S}_{3u}\mathrm{S}_{k}} + \frac{PE_{\mathrm{S}_{au}\mathrm{S}_{k}}}{PE_{\mathrm{S}_{3a}\mathrm{S}_{1}} + PE_{\mathrm{S}_{3a}\mathrm{S}_{2}} + PE_{\mathrm{S}_{3b}\mathrm{S}_{1}} + PE_{\mathrm{S}_{3b}\mathrm{S}_{2}}} ICS_{\mathrm{S}_{3a}\mathrm{S}_{3b}\mathrm{S}_{1}\mathrm{S}_{2}} \\ \text{for } (u,k) \in \{(a,1),\,(a,2),\,(b,1),\,(b,2)\}\,. \end{gathered} \tag{4}$$

Otherwise, if ICS occurred for photons that underwent IDS, the COG was used for the crystal positionings. Then, the event was considered as IDS (figure 4(a)), and IDS recovery was applied with equation (1).

2.3. Reconstruction

To reconstruct the images, we used histogram-based 3D ordered-subset expectation maximization with 18 subsets for each iteration. For spatial resolution measurements in section 2.1.2.2, the iteration numbers were

Table 2. Sensitivities and IDS occurrence rates of LSO and GAGG PET.

	LSO	GAGG
Sensitivity (kcps MBq^{-1})	5.81	2.52
Sensitivity with IDS recovery (kcps MBq^{-1})	6.78	3.35
IDS occurrence rate	17%	33%

Table 3. ICS occurrence and crystal mispositioning rates of 511 keV and IDS photon in LSO and GAGG PET.

		LSO	GAGG
ICS occurrence rate	511 keV photon	40%	53%
	IDS photon	16%	24%
Crystal mispositioning rate	511 keV photon	32%	43%
	IDS photon	12%	19%

3 and 5 for LSO and GAGG PET, respectively, which were determined to be where the values of the spatial resolutions started to saturate. For image quality measurements in section 2.1.2.3, we iterated the images until the noise levels of the images were acceptable. The voxel size of the output images was $0.5425 \times 0.5425 \times 0.5425$ mm^3 for spatial resolution measurement and $1.085 \times 1.085 \times 2.17$ mm^3 for image quality measurement.

We obtained uniform data with 511 keV back-to-back source distributed in a cylinder which had a diameter of 26 cm and an axial length of 20 cm for direct normalization. The normalization correction factor of each LOR was calculated as an inverse of the count from the uniform source acquisition, and the factor was multiplied to the count from the phantom acquisition to compensate geometrical sensitivity mapped in the image space. When applying IDS recovery, non-IDS and IDS events were recorded separately for both uniform and phantom data. Non-IDS phantom data were normalized with non-IDS uniform data, while IDS phantom data were normalized with IDS uniform data. The same procedure was used for the ICS recovery. Attenuation corrections were also applied with analytic attenuation maps. The phantom-scattered events and random coincidences were rejected based on the simulation output for both uniform and phantom data. We did not apply any resolution modeling or post-filtering in the reconstruction process.

2.4. Image quality analysis

The quality of the reconstructed images of the lesion phantom described in section 2.1.2.3 was quantitatively evaluated using the NEMA NU2-2007 protocol (National Electrical Manufacturers Association 2007). The contrast recovery coefficient (CRC) and background variability (BV) of each lesion i were measured as follows:

$$\begin{aligned} \mathrm{CRC}_{\mathrm{hot},i} &= \frac{\mu_{hot,i}/\mu_{bckg}-1}{C_{hot}-1} \times 100\%, \\ \mathrm{CRC}_{\mathrm{cold},i} &= \left(1-\mu_{cold,i}/\mu_{bckg}\right) \times 100\% \\ \mathrm{BV}_i &= \sigma_i/\mu_{bckg} \end{aligned}$$

where μ denotes the mean pixel intensity in each region-of-interest (ROI). The activity concentration ratio of the hot lesion to the background, C_{hot}, was equal to 3 in this study. σ_i is the standard deviation of the pixel values of the ROI drawn in the background region which had the same size as that of the ith lesion.

3. Results

3.1. IDS and ICS occurrence rates

Using only double coincidences, the measured sensitivities of LSO and GAGG PET were 5.81 and 2.52 kcps MBq^{-1}, respectively (table 2) with the 511 keV back-to-back rod source. The sensitivity increment due to IDS recovery, which indicates IDS occurrence rate, was roughly two times higher in GAGG PET than in LSO PET. The ICS occurrence rate was also higher in GAGG PET, as expected (table 3). When the COG was used in GAGG PET, 43% of the single 511 keV events were positioned to the wrong crystals due to ICS in our crystal block geometry. Both ICS occurrence and crystal mispositioning rates were lower for IDS photons (i.e. photons which interacted at S_1 and S_2 in figure 4) than 511 keV photons because photoelectric absorption is relatively dominant compared to Compton scattering for photons with low energy.

In the same setup, we investigated proportions of event types to be recovered in double coincidences and IDS events (table 4), which were similar to the values estimated using the results in table 3. In GAGG PET, for example, 50% and 28% of the double coincidences were 1 ICS and 2 ICS events, therefore were recovered using equations (2) and (3), respectively. 51% of the IDS, of which ICS occurred for non-IDS photon as

Table 4. Proportions of event types in double coincidences and IDS events.

	Event type	LSO	GAGG
Double coincidence	PE pair	37%	22%
	1 ICS[a]	47%	50%
	2 ICS[b]	16%	28%
IDS	ICS for non-IDS photon[c]	38%	51%
	Otherwise	62%	49%

[a]Figure 4(b) top.
[b]Figure 4(b) bottom.
[c]Figure 4(c).

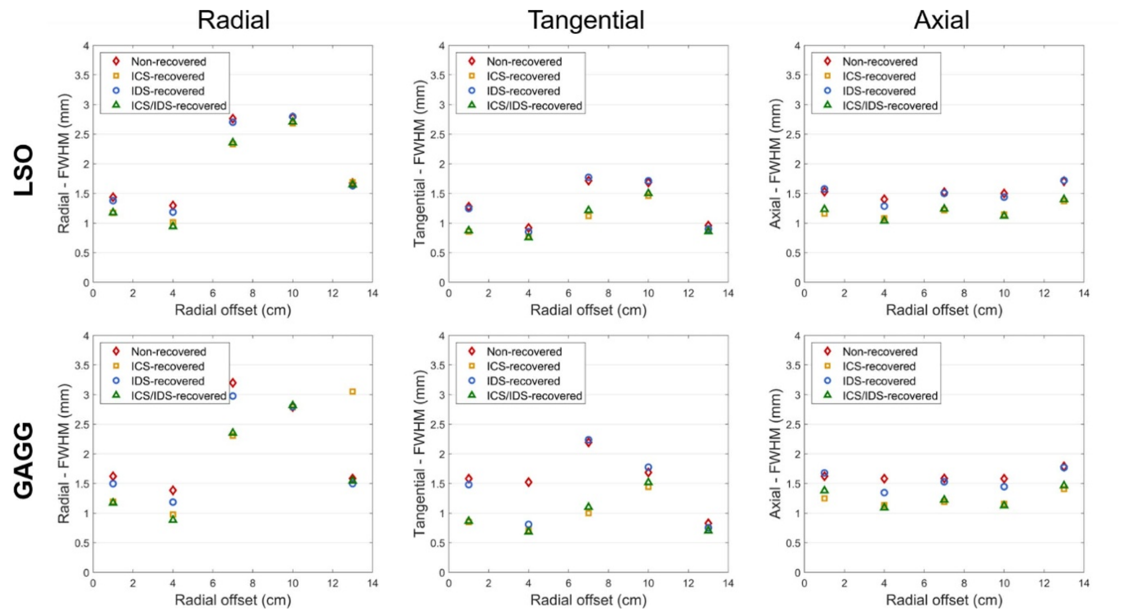

Figure 5. Radial, tangential, and axial resolutions in LSO and GAGG PET with IDS or ICS recovery differing radial offset of the point source.

shown in figure 4(c), were recovered with equation (4), while remaining events were recovered with equation (1), ignoring the ICS of IDS photons.

3.2. Spatial resolution

The radial, tangential, and axial spatial resolutions of GAGG PET and LSO PET are shown in figure 5. Compared to the non-recovered images, IDS recovery showed an insignificant impact on spatial resolution. ICS recovery improved the spatial resolution for all three directions. When ICS recovery was not applied, GAGG PET showed worse resolution than LSO PET. However, with ICS recovery, both PET showed comparable resolutions with an improvement of GAGG larger than that of LSO. As the geometry and acquisition setup were identical except for the crystal material, the results imply that blurring of the point spread was efficiently reduced by ICS recovery.

3.3. Image quality

3.3.1. Lesion phantom

The reconstructed images of the lesion phantom with IDS or ICS recovery applied are shown in figure 6. Mean pixel intensities increased when IDS recovery was applied due to high sensitivity, while ICS recovery enhanced the overall visibility of both hot and cold lesions.

Figure 7 shows the measured CRC and BV of each lesions in the reconstructed images with number of iterations of 1 to 5. Higher CRC was achieved with ICS recovery, especially in small lesions. However, BV was degraded in the ICS-recovered images with an increase in noise: in-depth discussions are stated in section 4. IDS recovery slightly improved BV while preserving CRC. Degradation of BV by ICS recovery was relieved when both ICS and IDS recoveries were applied. The degree of impact was larger in GAGG PET than in LSO PET because of the higher occurrence rates of IDS and ICS.

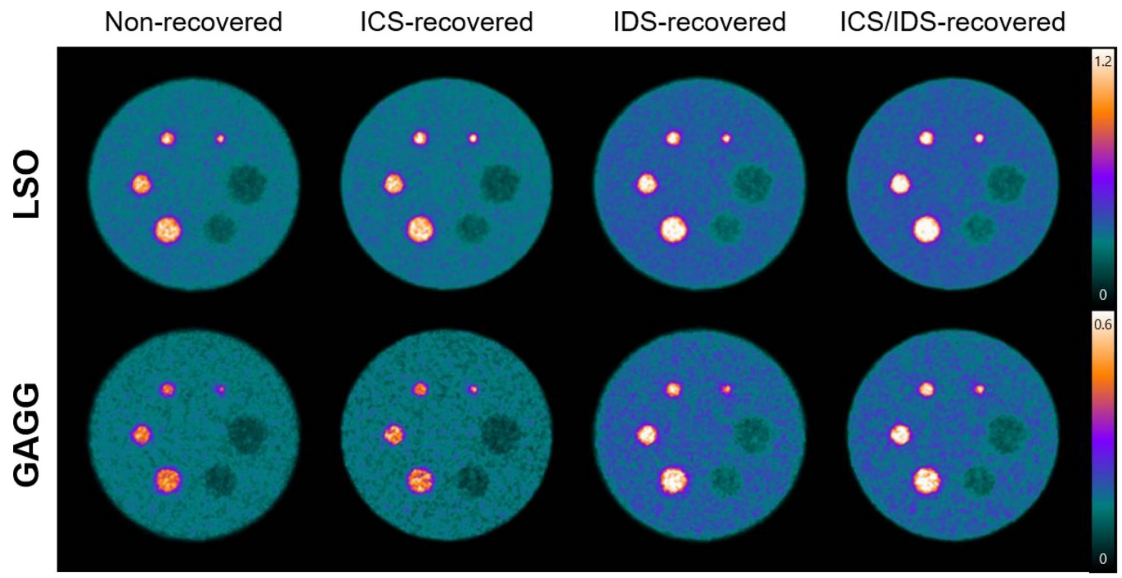

Figure 6. Reconstructed images of the lesion phantom with IDS or ICS recovery in LSO and GAGG PET (2 iterations, 18 subiterations).

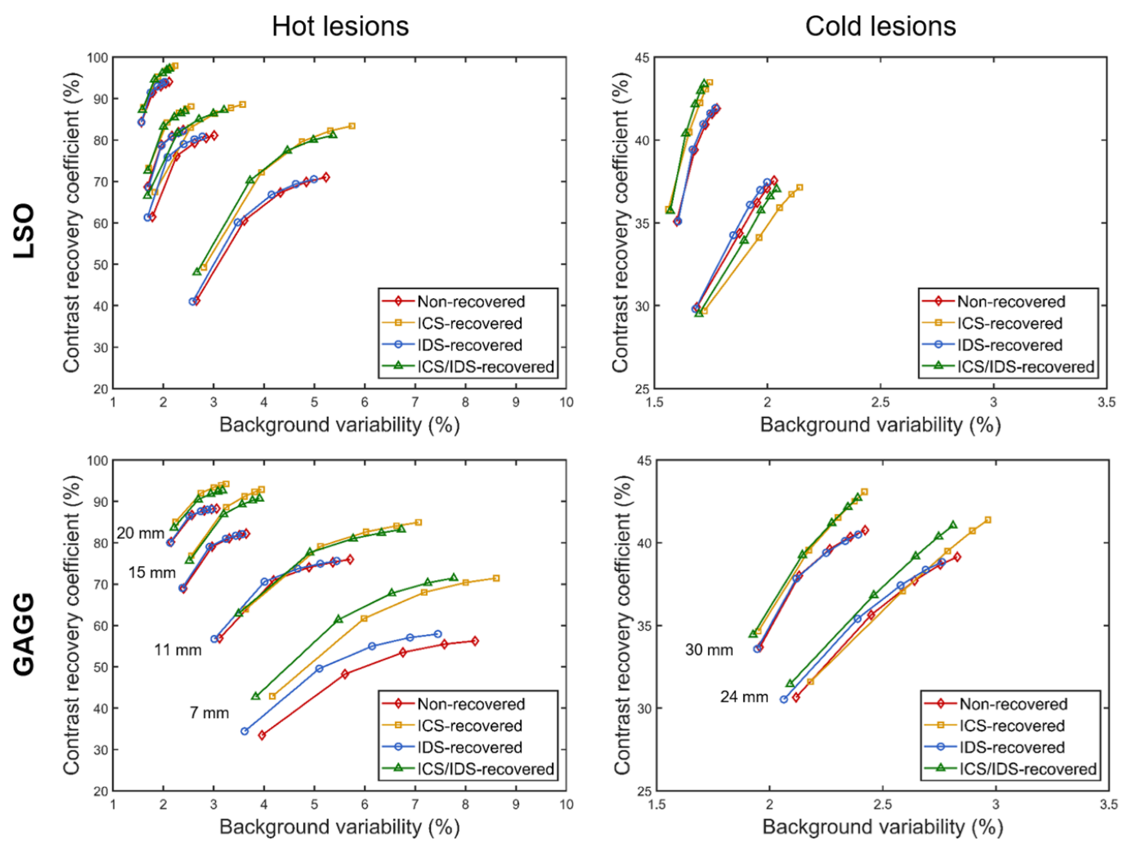

Figure 7. CRC versus BV curves of the hot and cold lesions measured from the lesion phantom images. Data points in upward direction correspond to the iteration numbers of 1 to 5 in order.

3.3.2. Hot-rod phantom

The small rods were well resolved in images with ICS recovery shown in figure 8 for both LSO and GAGG. When no recovery was applied, the 1.5 mm rods were not clear in GAGG PET image compared to LSO PET image. However, the visibilities were comparable in ICS-recovered images, which could be resulted by spatial resolution recovery effect discussed in section 3.2. The line profiles of ICS-recovered images in figure 9 also show better peak-to-valley ratio of the pixel intensities.

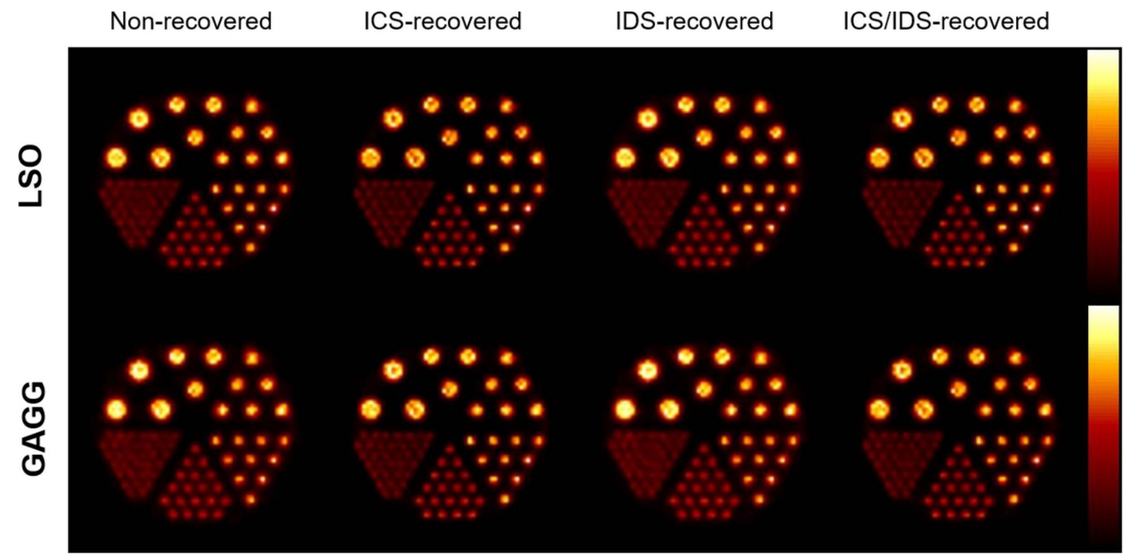

Figure 8. Reconstructed images of hot-rod phantom with IDS or ICS recovery in the LSO and GAGG PET (10 iterations, 18 subiterations). Image scale was selected to cover the full range of the pixel values for each image.

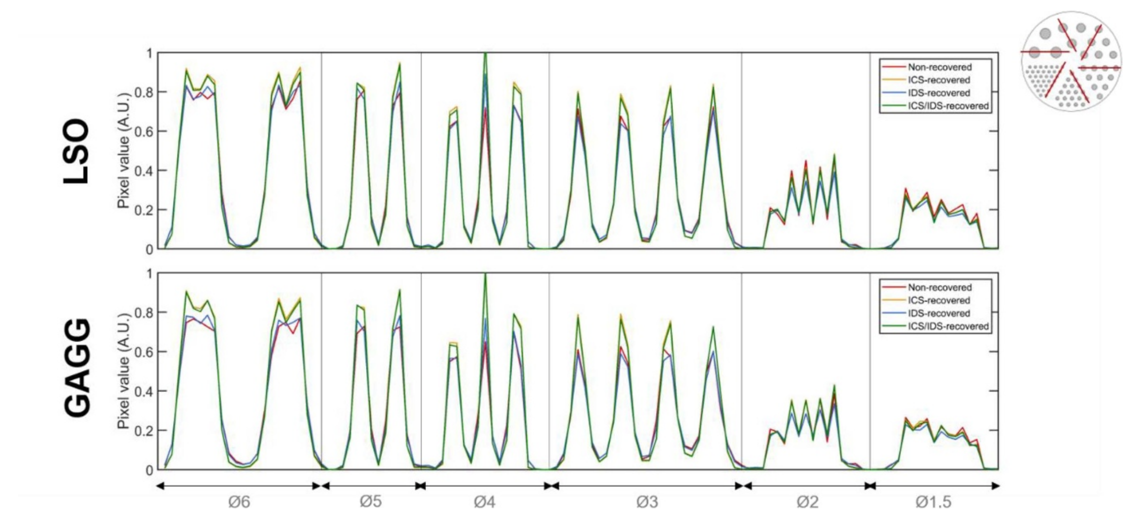

Figure 9. Line profiles of the hot-rod phantom images with IDS or ICS recovery in the LSO and GAGG PET. The vertical lines in the figure indicate the boundaries between the line profiles for different rod diameters.

3.3.3. Hoffman phantom

As shown in figure 10, when ICS recovery was applied, the detailed structures of the 2D Hoffman phantom were more clearly shown with the sharpened boundaries. The enhancement of the visibility was significant in GAGG owing to a frequent crystal mispositioning induced by ICS. Figure 11 also show that ICS recovery improved the overall contrast of the image. IDS- and ICS/IDS-recovered images were slightly less noisy than non-recovered and ICS-recovered images, respectively.

4. Discussion

We estimated the increment of sensitivity by adding IDS events to practical double coincidences in the brain-sized PET. When using the same LSO crystals, IDS was less frequently detected in brain PET than small-animal PET which was tested in the previous study (Lee *et al* 2018b). In the brain PET geometry, the sectors were placed far from each other, and both the block size and the gaps between the blocks were relatively large compared to the compact small-animal PET. On the contrary, the long axial length would be the factor that increases the IDS occurrence rate because IDS events along the axial direction are detected.

We extended the proportional method, which has been used for IDS recovery, to ICS recovery. As a result, improved visibility of the lesions and details owing to improvement in spatial resolution were shown in both

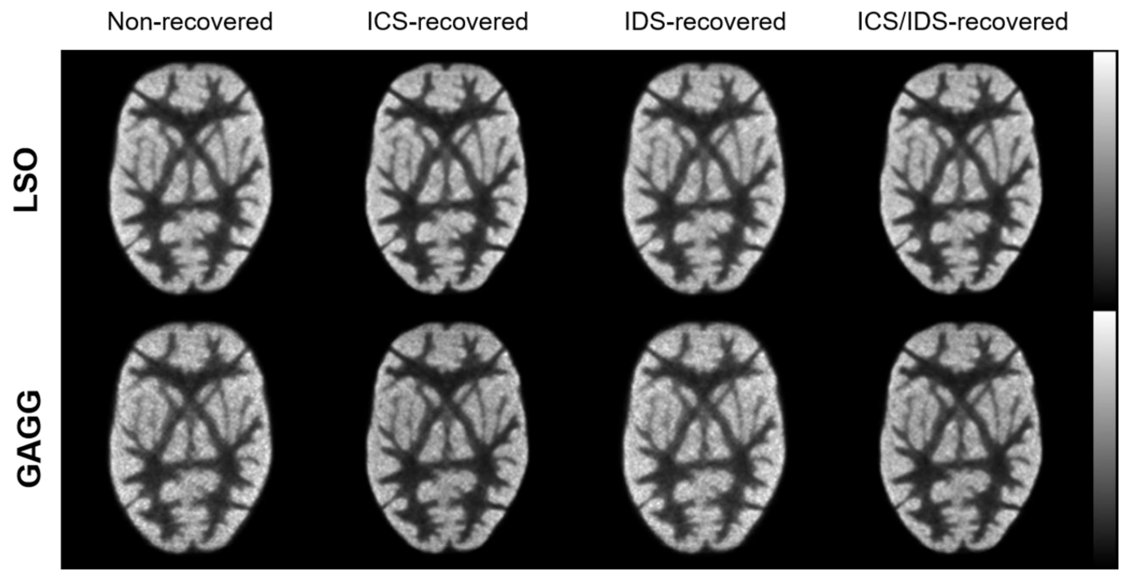

Figure 10. Reconstructed images of 2D Hoffman phantom with IDS or ICS recovery in LSO and GAGG PET (2 iterations, 18 subiterations). The image scale was selected to cover the full range of the pixel values for each image.

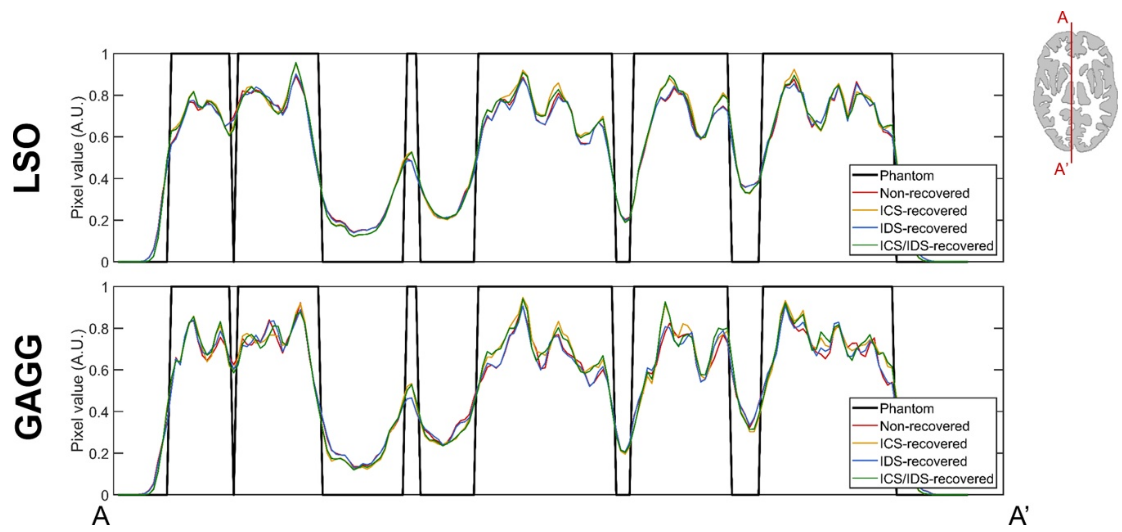

Figure 11. Line profiles of 2D Hoffman phantom images with IDS or ICS recovery in LSO and GAGG PET.

the lesion phantom and Hoffman phantom. However, degradation of BV was also shown: as the proportional method for ICS recovery is based on the number of LORs in which both photon interactions were PE, the performance of the recovery would be highly dependent on the statistics of those LORs. In this study, the noise level of the images increased because the number of LORs of the PE pairs was insufficient. However, the degradation of BV was alleviated by applying IDS recovery. Further development is required for a reliable implementation of the proportional method to recover ICS events. The proportional method for ICS recovery would be easily applicable to the PET systems using individual readout which are able to discriminate whether an event is ICS or not and record the interacted crystals of the ICS events (Shimazoe *et al* 2013, Omidvari *et al* 2017, Ahnen *et al* 2018, Chen *et al* 2018).

Comparing GAGG to LSO, as both IDS and ICS occurred frequently, the impact of the recoveries on image quality was significant. IDS recovery largely alleviated the limitation in the sensitivity of GAGG PET. The spatial resolution of GAGG PET was comparable to that of LSO PET with ICS recovery, which indicated that the effect of ICS on point spread was recovered. ICS was posed as a problem in previous studies that developed PET scanners using detector materials with low stopping power such as GAGG (Schneider *et al* 2015) and cadmium zinc telluride (Pratx and Levin 2009, Abbaszadeh *et al* 2018). In this study, we showed that IDS and ICS recovery would be a promising strategy to improve the overall performance and image quality, especially for low-density and low-Z material-based PET. Meanwhile, some systems with low-Z crystals which utilize ICS to combine Compton imaging with PET are under development (Kuramoto *et al* 2017, Shimazoe *et al* 2020). We expect that the ICS recovery technique used in this study might provide some clues to improve the Compton reconstruction, such as proportional weightings of the Compton cones to enhance image quality and increase sensitivity.

To implement the IDS and ICS recoveries in real PET, several corrections would be required for quantitative imaging. Scatter corrections would be applied to respective normalization and phantom data using tail fitting or single scatter simulation techniques. In case of random correction, random triple coincidences of which three 511 keV photons are involved would be effectively rejected by applying the energy window mentioned in section 2.2.1 and figure 3. The remaining random events can be simply corrected by conventional delayed time window technique. Non-ICS, ICS, IDS, and IDS + ICS events would be separately recorded with applying a single delayed window, and random counts of each event type would be estimated based on the identical calculations for recoveries, then subtracted from the prompt counts. As the practical corrections were beyond the scope of this study which was to investigate effect of ICS and IDS recoveries, we simply used simulation results to reject scatter and random events. The detailed correction techniques will be thoroughly studied in further implementation and validation of the recoveries in the real system.

5. Conclusion

We implemented IDS and ICS recoveries to brain PET using the proportional method to improve the performance and image quality of PET. As IDS recovery increased the sensitivity, BV improved while CRC was preserved in the reconstructed images. ICS recovery improved the spatial resolution, which eventually improved CRC and lesion detectability of the images. The impact of IDS and ICS recoveries was significant in GAGG-based PET because GAGG induced frequent Compton scattering compared to LSO. We suggest that the proportional method would be suitable for IDS and ICS recoveries of PET. In addition, we emphasize the importance of the recoveries for PET using crystals with low stopping power.

Acknowledgments

This work was supported by grants from the National Research Foundation of Korea (NRF) funded by the Korean Ministry of Science and ICT (Grant Nos. NRF-2016R1A2B3014645).

ORCID iD

Jae Sung Lee https://orcid.org/0000-0001-7623-053X

References

Abbaszadeh S, Chinn G and C S L 2018 Positioning true coincidences that undergo inter-and intra-crystal scatter for a sub-mm resolution cadmium zinc telluride-based PET system *Phys. Med. Biol.* **63** 025012

Ahnen M *et al* 2018 Performance measurements of the SAFIR prototype detector with the STiC ASIC readout *IEEE Trans. Radiat. Plasma Med. Sci.* **2** 250–8

Berger M J, Hubbell J H, Seltzer S M, Chang J, Coursey J S, Sukumar R, Zucker D S and Olsen K 2010 NIST XCOM: photon cross sections database (http://www.nist.gov/pml/data/xcom/index.cfm)

Chen Y, Deng Z and Liu Y 2018 DIET: a multi-channel SiPM readout ASIC for TOF-PET with individual energy and timing digitizer *J. Instrum.* **13** P07023

Comanor K A, Virador P R G and Moses W W 1996 Algorithms to identify detector Compton scatter in PET modules *IEEE Trans. Nucl. Sci.* **43** 2213–8

Ferri A, Gola A, Serra N, Tarolli A, Zorzi N and Piemonte C 2014 Performance of FBK high-density SiPM technology coupled to Ce:LYSO and Ce:GAGG for TOF-PET *Phys. Med. Biol.* **59** 869–80

Frach T, Prescher G, Degenhardt C, De Gruyter R, Schmitz A and Ballizany R 2009 The digital silicon photomultiplier - principle of operation and intrinsic detector performance *2009 IEEE Nuclear Science Symp. Conf. Record* (Piscataway, NJ: IEEE) pp 1959–65

Gillam J E, Solevi P, Oliver J F, Casella C, Heller M, Joram C and Rafecas M 2014 Sensitivity recovery for the AX-PET prototype using inter-crystal scattering events *Phys. Med. Biol.* **59** 4065–83

Hsu D F C, Freese D L, Innes D R and Levin C S 2019 Intercrystal scatter studies for a 1 mm^3 resolution clinical PET system prototype *Phys. Med. Biol.* **64** 090524

Jan S *et al* 2004 GATE: A simulation toolkit for PET and SPECT *Phys. Med. Biol.* **49** 4543–61

Kamada K, Yanagida T, Endo T, Tsutumi K, Usuki Y, Nikl M, Fujimoto Y, Fukabori A and Yoshikawa A 2012 2 inch diameter single crystal growth and scintillation properties of Ce:$Gd_3Al_2Ga_3O_{12}$ *J. Cryst. Growth* **352** 88–90

Kobayashi T, Yamamoto S, Okumura S, Yeom J Y, Kamada K and Yoshikawa A 2017 Basic performance of Mg co-doped new scintillator used for TOF-DOI-PET systems *Nucl. Instrum. Methods Phys. Res.* A **842** 14–19

Kuramoto M, Nakamori T, Kimura S, Gunji S, Takakura M and Kataoka J 2017 Development of TOF-PET using Compton scattering by plastic scintillators *Nucl. Instrum. Methods Phys. Res.* A **845** 668–72

Kwon S Il *et al* 2011 Development of small-animal PET prototype using silicon photomultiplier (SiPM): initial results of phantom and animal imaging studies *J. Nucl. Med.* **52** 572–9

Lage E, Parot V, Moore S C, Sitek A, Udías J M, Dave S R, Park M-A, Vaquero J J and Herraiz J L 2015 Recovery and normalization of triple coincidences in PET *Med. Phys.* **42** 1398–410

Lee M S, Kang S K and Lee J S 2018a Novel inter-crystal scattering event identification method for PET detectors *Phys. Med. Biol.* **63** 115015

Lee S, Lee M S, Kim K Y and Lee J S 2018b Systematic study on factors influencing the performance of interdetector scatter recovery in small-animal PET *Med. Phys.* **45** 3551–62

Lee Y-S, Leem H-T, Yamamoto S, Choi Y, Kamada K, Yoshikawa A, Park S-G and Yeom J-Y 2016 Digital silicon photomultiplier readout of a new fast and bright scintillation crystal (Ce:GFAG) *Nucl. Instrum. Methods Phys. Res.* A **832** 63–67

Michaud J B, Tétrault M A, Beaudoin J F, Cadorette J, Leroux J D, Brunet C A, Lecomte R and Fontaine R 2015 Sensitivity increase through a neural network method for LOR recovery of ICS triple coincidences in high-resolution pixelated-detectors PET scanners *IEEE Trans. Nucl. Sci.* **62** 82–94

National Electrical Manufacturers Association 2007 Performance measurements of positron emission tomographs *NEMA Standards Publication NU 2-2007* (Rosslyn, VA: National Electrical Manufacturers Association)

Omidvari N, Cabello J, Topping G, Schneider F R, Paul S, Schwaiger M and Ziegler S I 2017 PET performance evaluation of MADPET4: a small animal PET insert for a 7 T MRI scanner *Phys. Med. Biol.* **62** 8671–92

Pratx G and Levin C S 2009 Bayesian reconstruction of photon interaction sequences for high-resolution PET detectors *Phys. Med. Biol.* **54** 5073–94

Rafecas M, Böning G, Pichler B J, Lorenz E, Schwaiger M and Ziegler S I 2003 Inter-crystal scatter in a dual layer, high resolution LSO-APD positron emission tomograph *Phys. Med. Biol.* **48** 821–48

Schneider F R, Shimazoe K, Somlai-Schweiger I and Ziegler S I 2015 A PET detector prototype based on digital SiPMs and GAGG scintillators *Phys. Med. Biol.* **60** 1667–79

Shao Y, Cherry S R, Siegel S and Silverman R W 1996 A study of inter-crystal scatter in small scintillator arrays designed for high resolution PET imaging *IEEE Trans. Nucl. Sci.* **43** 1938–44

Shimazoe K, Orita T, Nakamura Y and Takahashi H 2013 Time over threshold based multi-channel LuAG-APD PET detector *Nucl. Instrum. Methods Phys. Res.* A **731** 109–13

Shimazoe K, Yoshino M, Ohshima Y, Uenomachi M, Oogane K, Orita T, Takahashi H, Kamada K, Yoshikawa A and Takahashi M 2020 Development of simultaneous PET and Compton imaging using GAGG-SiPM based pixel detectors *Nucl. Instrum. Methods Phys. Res.* A **954** 161499

Siegel S, Silverman R W, Shao Y and Cherry S R 1996 Simple charge division readouts for imaging scintillator arrays using a multi-channel PMT *IEEE Trans. Nucl. Sci.* **43** 1634–41

Stewart A G, Seitz B, O'Neill K, Wall L and Jackson J C 2016 Energy resolution of Ce:GAGG and Pr:LuAG scintillators coupled to 3 mm × 3 mm silicon photomultipliers *IEEE Trans. Nucl. Sci.* **63** 2496–501

Surti S and Karp J S 2018 Impact of event positioning algorithm on performance of a whole-body PET scanner using one-to-one coupled detectors *Phys. Med. Biol.* **63** 055008

Teimoorisichani M and Goertzen A L 2019 A study of inter-crystal scatter in dual-layer offset scintillator arrays for brain-dedicated PET scanners *Phys. Med. Biol.* **64** 115007

Wagadarikar A A, Ivan A, Dolinsky S and McDaniel D L 2012 Sensitivity improvement of time-of-flight (ToF)-PET detector through recovery of Compton scattered annihilation photons *IEEE Trans. Nucl. Sci.* **61** 121–5

Yeom J Y, Yamamoto S, Derenzo S E, Spanoudaki V C, Kamada K, Endo T and Levin C S 2013 First performance results of Ce:GAGG scintillation crystals with silicon photomultipliers *IEEE Trans. Nucl. Sci.* **60** 988–92

Yoshida E, Tashima H and Yamaya T 2014 Sensitivity booster for DOI-PET scanner by utilizing Compton scattering events between detector blocks *Nucl. Instrum. Methods Phys. Res.* A **763** 502–9

Zhang C, Sang Z, Wang X, Zhang X and Yang Y 2019 The effects of inter-crystal scattering events on the performance of PET detectors *Phys. Med. Biol.* **64** 205004